Research Article

Hamed Elmadah, Daniel Roger*, and Noureddine Takorabet

Design of inorganic coils for high temperature electrical machines

Abstract: The paper deals with a high frequency model of inorganic coils used to build high temperature (HT°) motor. The HT° wire has a nickel layer that protects the copper against oxidation and a thin inorganic coating, which has poor electrical and mechanical properties. Therefore, the coils must be designed with a special care for getting a good distribution of turn-to-turn voltage during the fast transients excited by the steep fronted voltages of the PWM inverter. A specific coil structure is proposed and a high frequency (HF) equivalent circuit able to compute the turn-to-turn voltages during transients. The voltage distribution between the coils of a stator phase is also detailed.

Keywords: Inorganic coils design, high frequency equivalent circuit, voltage spikes in stator coils

PACS: 41.20.-q, 81.05.-t

1 Introduction

Generally speaking, electrical machines are widely used for many applications because of their accurate torque control capabilities and high power volume ration. However, the organic nature of their electrical insulation system (EIS) has a limited operating temperature, which depends on the expected lifetime. This concept is defined in standards by the temperature index [1]. A lot of research has been done to push this limit [2–4]. The very high temperature environments are until now forbidden for machine made with organic EISs, except for applications requiring a very short life times as smoke evacuation during the first minutes of fires [5, 6].

For surpassing the temperature limit imposed by polymers, it is possible to use inorganic EIS made without any polymer. Large machines are designed with thick textile EIS made with mica and fiberglass [7]. For small compact machines, wires are insulated with a thin ceramic layer [8] of more or less $10\mu m$. This thin layer is not perfect; it has many microscopic cracks ($\leqslant 1\mu m$) [9]. For both cases, the high temperature (HT°) insulating layers are not waterproof, they cannot protect the copper wire against oxidation at it is performed at lower temperatures by polymers. A nickel layer is added on the copper wire for avoiding copper oxidation.

Compared to the standard organic enamelled wires, the HT° wires have poor mechanical and electrical properties. The maximum turn-to-turn voltage is more or less $200\,V_{RMS}$ at $500°C$ [9]. This limit must be compared to the usual values, which is more or less $600\,V_{RMS}$ for standard enameled wires at room temperature. Consequently for operating at standard voltages, the machine windings must provide a better voltage distribution between turns. The thin ceramic insulating layer is brittle; the wires must be protected by a HT° cement. Consequently, the inorganic coils are inflexible objects; this constraint must be considered for designing the stator core of HT° machines.

Soft magnetic laminated cores can operate up to $500°C$ when the designer accepts a slight reduction of the flux density. the magnetic sheets must be insulated by their natural oxidation [10, 11].

A recent studies dealing with HT° machines show the limits of each structure. For the induction motor, the first limit is the complex shapes required for the distributed windings [12, 13]. The second one is related to the rotor cage resistance which increases with temperature. The rotor losses increase the temperature and the resistance; this cumulative effect may cause a lack of stability in addition of a poor efficiency. These drawbacks do not exist with permanent magnet synchronous machines (PMSM). Moreover, the winding can be made with one coil per stator slot, which is convenient with rigid inorganic coils [14].

With an inorganic HT° concentrated winding, the temperature limit of the PMSM depends on the magnet. The only magnets able to operate up to $500°C$ are metallic ones, which have a very low coercive field, so they cannot

*Corresponding Author: Daniel Roger: Univ. Artois - EA4025, LSEE, 62400 Bethune, France; Email: daniel-roger@ieee.org
Hamed Elmadah: Univ.Lorraine - EA4366, GREEN-ENSEM, F54516 Vandoeuvre les Nancy, France
Noureddine Takorabet: Univ.Lorraine - EA4366, GREEN-ENSEM, F54516 Vandoeuvre les Nancy, France

be used in PMSMs. Only few specific alloys of samarium and cobalt can be used in PMSMs up to $300 - 350°C$, but the limits of a reduced coercive field at high temperatures must be accepted [15]. Moreover, the rotor design must be made considering the high electric conductivity of these metallic magnets, they must be fragmented for getting limited losses due to flux density harmonics [16].

For exceeding the maximum temperature imposed by magnets, the synchronous reluctance machine (SRM) topologies can be used. The stator is similar but the rotor is only made of soft magnetic materials [17]. This machine is magnetized by the stator currents, the filling factor of stator slots becomes a more critical element of the design.

For every HT° motor topologies, the poor insulation properties of the ceramic coated wire must be compensated by a specific turn arrangement in coils [18]. The paper proposes a winding structure which makes it possible to feed the machine with usual voltages produced by PWM inverters despite the poor electrical performances of the ceramic coated wire. The method for building these coils is developed. The electrical stress distribution inside the coils and between coils is analyzed with high frequency (HF) equivalent circuits.

2 Synchronous reluctant machine topology

The inorganic coils are rigid objects without any flexibility. The stator slots must be opened for accepting prefabricated coils. The stator teeth must have a cuboid shape adapted to rigid coils. Thereby, the machine must be a doubly salient synchronous reluctance one. For a three-phase motor, the combination 12 slots - 10 poles is widely used for many applications. The 12 stator coils are divided into 3 phases which gives 4 coils per phase. But, with cuboid teeth in a cylindrical stator, there is a fairly large empty space between coils at the bottom of each slot. With 24 smaller teeth, this lost space is divided by about 2.

It it not obvious to produce rotating magneto-motive force (mmf) able to interact with the rotor for producing an average torque with a 24-slot stator and a very simple winding made of one coil per slot. This problem has been deeply studied for designing fractional-slot concentrated winding usually made with standard enameled wires [19, 20]. The principle consists in applying Fourier series to the mmf produced by the currents in coils. This analysis is made with two variables: the position of any point in the machine air-gap and the time. The Fourier analysis shows the existence of many mmf components; the only useful one,

able to produce an average torque, must have a number of magnetic poles equal to the rotor mechanical poles. The other ones contribute to the torque ripple.

For a 3-phase 24-slot stator, the scientific literature offers 3 rotor possibilities for a doubly salient synchronous reluctance motor: 16 poles, 20 poles or 28 poles and the associates specific coil connections [20–23]. The torque ripple is an important parameter to consider; especially because large vibrations can damage the rigid inorganic coils. Consequently, it is important to choose a structure that limits the torque ripples without increasing the complexity of the prototype. 2D simulations by finite elements (FE) were made for the three topologies, with the same geometrical input. The simulations show that the lowest torque ripples are obtained with the configuration 24 coils - 28 poles. However, this configuration requires a higher electric frequency at imposed speed because this motor has a higher pole-pair number. Eddy currents losses in iron are higher. Thus, the choice of 24-20 configuration is an acceptable compromise, which has torque ripple lower than the 24-16 configuration. After choosing the topology 24-20, the shape of the rotor teeth must be chosen. An optimization approach is adopted considering three parameters: the angular rotor teeth θ width, the sides of teeth inclination α and air-gap extra thickness e. A parametric study made it possible to obtain elements that limit torque harmonics and the Figure 1 shows the three optimization parameters. Optimization results are $\theta = 8.1°$, $\alpha = 10°$ and $e = 0.05mm$ [24].

Two solution have been implemented a massive rotor (Figure 2) and a laminated one (Figure 3). The massive rotor is made of steel, longitudinal slits have been added in
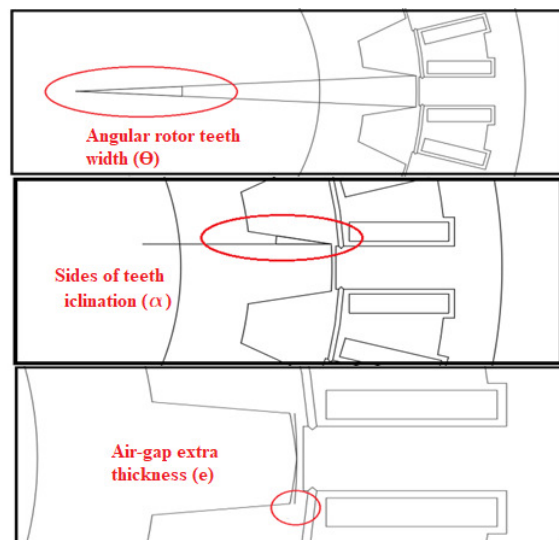

Figure 1: Rotor shape optimization parameters

Figure 2: Massive iron rotor with longitudinal slits for limiting eddy currents.
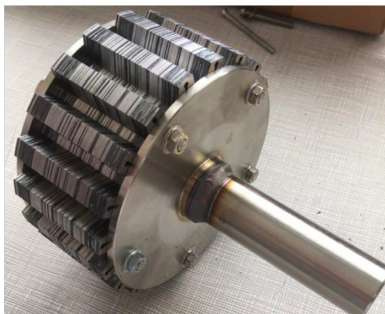

Figure 3: Laminated rotor made of FeSi magnetic sheets insulated by they natural oxidation.

the poles for limiting eddy currents due to rotating field harmonics. The laminated rotor is made of FeSi sheets insulated by their natural oxidation; their thicknesses is $0.5mm$. The massive rotor has the advantage of being very strong and relatively easy to build with today's machine tools. However, the main drawback of this technology is the higher eddy currents induced by the harmonic rotating fields. The laminated version is more difficult to manufacture; the FeSi sheets are cut by laser; they are compressed between two stainless steel flanges.

3 Structure of HT° inorganic coils

The brittle ceramic coated wires must be embedded in a HT° cement. The cement protect the conductors and contributes to the electrical isolation. The choice of a cement made of small grains (between $1\mu m$ and $44\mu m$) and a correct application procedure is a necessary procedure for filling the voids between turns. After the thermal cycles, this cement becomes very hard and protect the ceramic insulated wires [25]. However the turn-to-turn breakdown voltage remains much lower than for low temperature organic
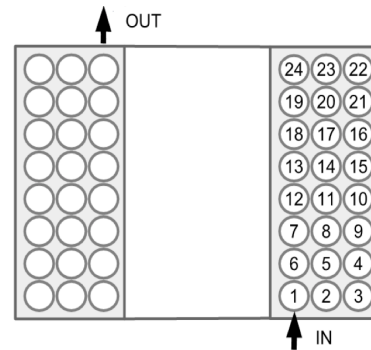

Figure 4: Turn position inside the HT° inorganic coil inspired form the high voltage transformer technology.

Figure 5: Plastic support defining the position of the tuns of a layer.

enameled wires [9]. A good voltage distribution between turns is compulsory; it is ensured by a specific turn arrangement. Figure 4 presents such an arrangement for a 24 turn coil made of 8 transverse layers of 3 adjacent turns. The input wire is at the beginning of the inner turn near the stator tooth. The position of the output wire depends on the layer number : for a even layer number the the output wire is near the stator tooth; for an odd one it at the end of the outer layer. With 8 layers of 3 turns, the maximum turn-to-turn voltage corresponds to the induced voltage in 5 turns.

This structure is realized with the plastic support of Figure 5 made by a 3D printer. The upper part defines the position of each turn in a layer; it can be removed from the lower part made of several "U" that correspond to the half of the stator slot width. When the upper part is removed, the three turn layer falls in the lower part of the plastic support. The picture of Figure 5 is made when the upper part is in the position for receiving the turns of an even layer; it is returned for making the odd ones. When the 8 layers have been placed in the lower part of the plastic support, they are carefully transferred in a stainless steel mold designed for defining the coil sizes. Figure 6 shows the mold containing a coil. The output wire is placed in front of the outer turn, for a even number of turn it must cross the end of the coil creating a small extra height of the coil end.

A strict protocol, based on the acquired experience and the instructions of the cement data sheet, must be ap-
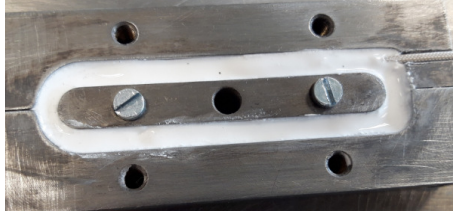
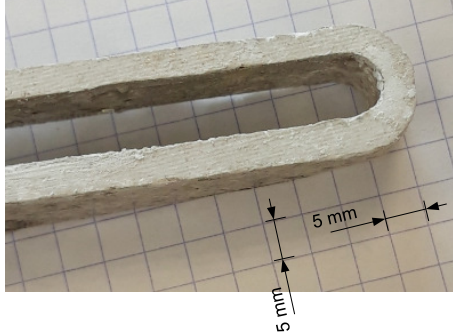**Figure 6:** Stainless steel mold defining the shape of inorganic coils.

5 mm

5 mm

Figure 7: Example of a HT° coil at the size of the 24-20 SRM prototype.
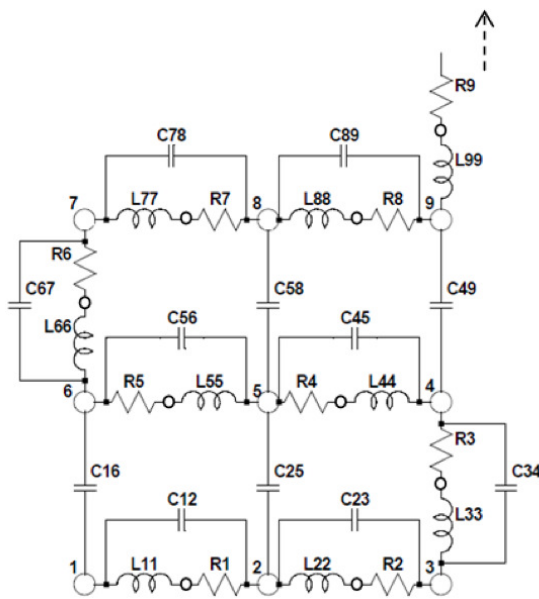

Figure 8: Spice equivalent circuit of a HT° coil.

plied for getting a coil without any crack and few residual voids. The cement hardening must be progressive in the mold. The process of cement grain growth, which makes the final hardness, is achieved by the last thermal cycle at 370°C. The 10 phases of the protocol can be summarized in the following list.

1. turn placing in the plastic support;
2. preparation of a small quantity of HT° cement;

3. laying a sheet of mica ($50\mu m$) on the internal walls of the mold;
4. transfer of the coil in the mold;
5. injection of the cement ;
6. 24 hours in a dry low pressure atmosphere;
7. first thermal cycle of 7 hours at $50°C$;
8. second thermal cycle of 5 hours at $70°C$;
9. third thermal cycle of 2 hours at $120°C$;
10. final hardening cycle of 4 hours at $370°C$.

Figure 7 shows an example for HT° coil. Small surface irregularities subsist, they are cause by an imperfect injection of cement into the mold. However the coils are very hard objects without any deep crack; it is very difficult to scratch them with a screwdriver.

4 Turn-to-turn voltage distribution in a coil

4.1 Fast phenomena analysis with an equivalent circuit

Transient phenomena due to the fast-fronted voltage of PWM patterns. These fast phenomena can be analyzed with a full wave 3D electromagnetic model. This approach is rather complex and time consuming; a simpler one can be used considering that each turn of the coil is much shorter than the wave length at the the highest frequency of the analysis. In these conditions, the analysis can be made with equivalent circuits defined at the turn level. Supposing that the wave length must be at least 10 times the average turn length, the minimum wave length is $1.2\ m$. For an insulating material, which permittivity is 10, the propagation speed of a plane wage is $95\ 10^6\ m/s$; the maximum frequency for the analysis at the turn level is $79\ MHz$, which is very high for the transient analysis of a motor coil.

Each turn is considered as an indivisible entity coupled to the others by the magnetic field (self and mutual inductances), and electric fields (capacitances). Figure 8 shows the part of this equivalent circuit corresponding to the first 9 turns of the HT° coil. The nodes with a number are the turns inputs defined in Figure 4. For each turn, an additional node connects the equivalent resistance representing the HF losses. The mutual inductances between turns are not presented but they are taken into account by a 24x24 inductance matrix. This equivalent circuit can be simulated by a Spice processor.
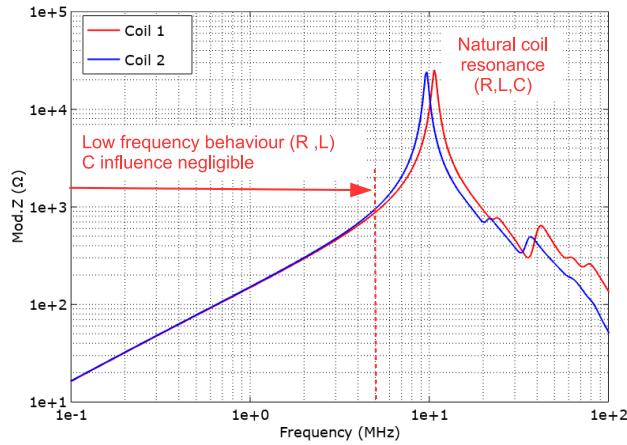
Figure 9: Impedance spectra of two HT° coils. The main resonance is at more or less 10 Hz.

Figure 9 shows the impedance modulus of two inorganic coils measured with an impedance analyzer from 100kHz to 100MHz. The curves are superimposed up to about 5MHz; the natural frequencies are very close to 10MHz, with a small difference due to variations of the actual turn positions which change the turn-to-turn capacitances. The main phenomena are observed at about 10 MHz, which is much under the model principle limit. The transient analysis can be made with wit an equivalent circuit built at the turn level.

The capacitances values are estimated using a specific coil made of two unconnected sets of 2 layers of 3 turns is used as a test bench. The building process is the same. Because of the 3 adjacent turns of the test bench, the turn-to-turn capacitance, estimated to 1/3 of the experimental value, is 7 pF. This value is confirmed by a 2D electrostatic simulation of two adjacent ceramic coated wires placed in a HT° cement.

4.2 Magnetic couplings

The inductance matrix is computed by a linear magneto-harmonic 2D finite element simulation. The laminated magnetic tooth in the center of the coil is not taken into account because a short experimental investigations shows that the coil natural frequency does not change significantly when it is placed on a stator tooth. This phenomena is explained by the strong skin effect in the stator magnetic tooth [26]. It is considered for the analysis made at the level of the full stator winding. However the influence of the nickel layer protecting the copper from oxidation is considered. The mesh must be very thin in the nickel layer for taking skin effects into account. The size of the mesh
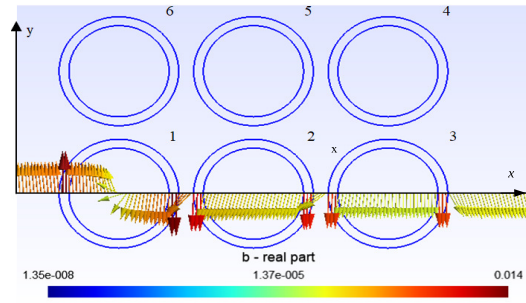

Figure 10: Color map of the flux density produced by $1A_{peak}$ in the turn 1.
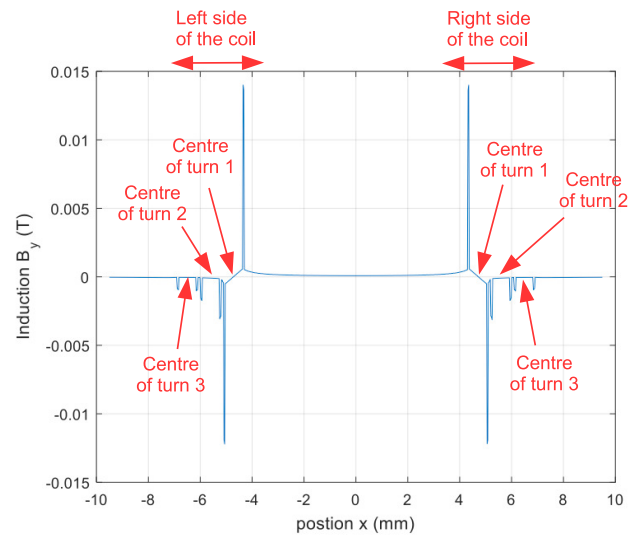

Figure 11: Y component of the flux density along a straight line at the center of the first layer for $1A_{peak}$ in turn 1.

must under 1/3 of the estimated skin depth in nickel. By supplying a single turn, the self-inductance and mutual inductances are determined by calculating the flux of each turn.

The materials are supposed linear and defined by their resistivities and relative permeabilities (ρ = 1.72 10^{-8} $\Omega.m$ and μ_R = 1 for the copper; ρ = 8.7 10^{-8} $\Omega.m$ and μ_R = 25 for the nickel [27]); the thickness of the nickel layer is 65 μm; the wire diameter is 1 mm. Figures 10 and 11 show the simulation results when the first turn is supplied by a sine current of 1 A peak. These figures show the flux density at $t = 0$, which is null at the centre points of the fed wires; it is positive inside the coil and negative outside. The nickel layer of each wire concentrates the flux density because of its relative permeability. This concentration has an influence on the inductance values and on losses.

Generally speaking, the inductance between the turns i and j, L_{ij}, is defined as the ratio between the magnetic

flux ϕ_j in the tun j and a current I_i in the same turn ($i = j$, self inductance) of in another one ($i \neq j$, mutual inductance) (1). Noting l the length of the coil and neglecting the end effects, the flux in a turn is given by (2).

$$L_{ij} = \frac{\phi_j}{I_i} \qquad (1)$$

$$\phi = \int B(x)\, l \, dx \qquad (2)$$

The inductance matrix is computed using (2) and (1) when a current I flows in the single turn i. The eddy currents in the nickel layers create a phase shift between the flux and the current; consequently, (1) yields a complex number that imaginary parts are not always negligible. Table 1 presents the self inductance of the turn 1 and the 23 mutual inductances between the turn 1 and the others ones. The imaginary parts can be neglected for turns far from the fed one (over the 4th layer). Results are similar for results obtained when another turn is fed. Computations has been made at several frequencies between $100\,kHz$ and $800\,kHz$, for the frequencies range where the turn-to-turn capacitance effects can be neglected. At these frequencies, the inductances matrix is almost constant.

Table 1: Self and mutual inductances relative to the first turn

layer	inner turn	middle turn	outer turn
1	$163 - j11.6\,nH$	$54.3 - j2.2\,nH$	$35.0 - j1.0\,nH$
2	$53.1 - j2.3\,nH$	$45.2 - j2.3\,nH$	$31.4 - j0.5\,nH$
3	$32.6 - j0.5\,nH$	$31.3 - j0.4\,nH$	$25.0 - j0\,nH$
4	$22.5 - j0\,nH$	$22.4 - j0\,nH$	$19.8 - j0\,nH$
5	$16.3 - j0\,nH$	$16.6 - j0\,nH$	$15.4 - j0\,nH$
6	$12.2 - j0\,nH$	$12.5 - j0\,nH$	$12.2 - j0\,nH$
7	$9.0 - j0\,nH$	$9.5 - j0\,nH$	$9.6 - j0\,nH$
8	$6.6 - j0\,nH$	$7.1 - j0\,nH$	$7.4 - j0\,nH$

Since all the imaginary parts are negative, the notation adopted is $\underline{L}_{ij} = L_{ijR} - jL_{ijI}$. The physical meaning of the inductance imaginary parts can be explained with an example that considers only the first turn and its impedance $\underline{Z}_1$ (3). It can be seen that the real part of the inductance produce the classical imaginary part of the impedance while the imaginary part correspond to a resistance due to eddy currents.

$$\underline{Z}_1 = j\underline{L}_{11}\omega = j\omega L_{11R} + \omega L_{11I} \qquad (3)$$

The real parts of the inductance matrix correspond to the L_{ii} elements of the spice equivalent circuit presented in Figure 8 and of the magnetic couplings between these elements. The imaginary parts are used for estimating the R_i resistance values. These values are supposed to be the same for each turn. The turn resistance value is estimated neglecting the influence of the turn-to-turn capacitances. With this hypothesis, Figure 8 shows that the current is the same in all the turns. The matrix formulation (4) becomes simpler because $I_1 = I_2 = \ldots = I_{24}$; the total flux $\underline{\psi}$ is $\underline{\psi} = \underline{\phi}_1 + \ldots + \underline{\phi}_{24}$; therefore (5) gives the equivalent complex inductance $\underline{L}$ of the coil.

$$\begin{bmatrix} \underline{\phi}_1 \\ . \\ \underline{\phi}_{24} \end{bmatrix} = \begin{bmatrix} \underline{L}_{1,1} & \cdots & \underline{L}_{1,24} \\ . & \cdots & . \\ \underline{L}_{24,1} & \cdots & \underline{L}_{24,24} \end{bmatrix} \cdot \begin{bmatrix} I_1 \\ . \\ I_{24} \end{bmatrix} \qquad (4)$$

$$\underline{L} = \frac{\underline{\psi}}{I} = \sum_{i,j=1}^{24} \underline{L}_{i,j} \qquad (5)$$

The turn resistance is the sum of the dc resistance R_{dc} and the effect of the imaginary part of the equivalent inductance. For a 24-turn coil this resistance is estimated by (6).

$$R = \frac{1}{24}\left[R_{dc} + \omega \Im(\underline{L}) \right] \qquad (6)$$

The experimental verification is not possible at the turn level because of the parasitic inductances introduced by connection wires. Therefore, it is made at the coil level comparing the global impedance computed with Spice and the measured one with an impedance analyzer. Results are presented in Figure 12
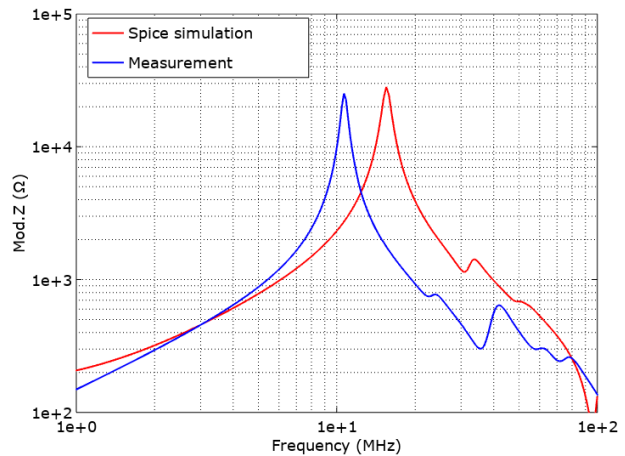

Figure 12: Spice model validation by a spectrum analysis of a whole coil.

The differences between the computed impedance and the measured one can be interpreted by the difficult estimation of the turn-to-turn capacitance, which depends on the average distances between turns.
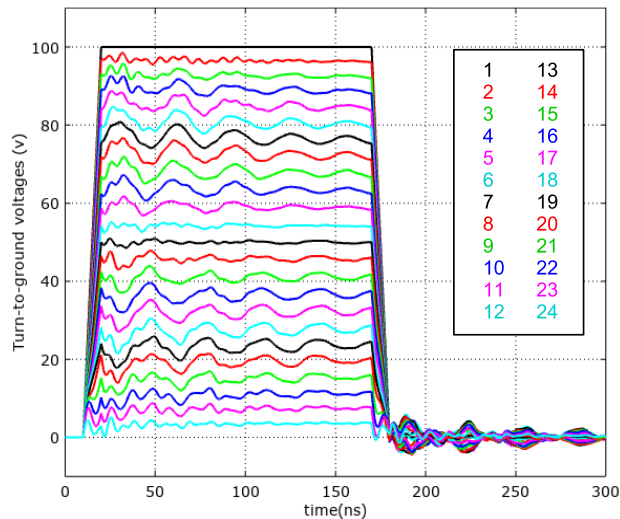
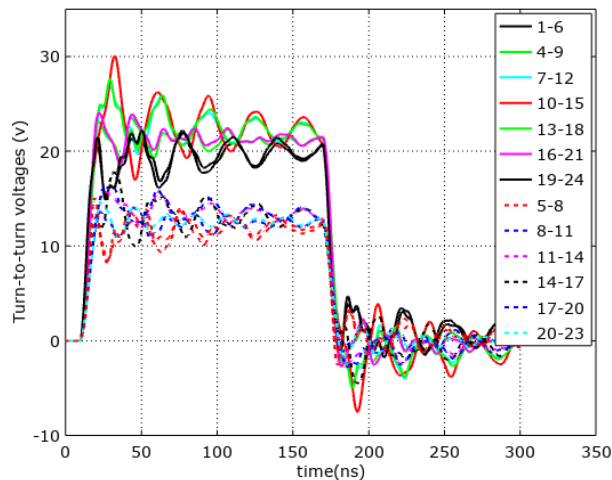**Figure 13:** Transient voltage at the nodes of the Spice equivalent circuit.

Figure 14: Transient turn-to-turn voltage for a coil voltage pulse of $100\,V$.

The Spice model is used for computing the turn-to-ground voltage at each node of the equivalent circuit. Results are presented in Figure 13 for an input voltage of $100\,V$ – $150\,ns$ pulse imposed between the first turn input and the last one output. The rise and a fall times are set to $10\,ns$. The steady states are nearly reached at the end of the pulse; they show a linear voltage distribution between turns with steps of $1/24$ (4.16%) of the pulse voltage.

The turn-to-turn voltages at any points of the coil are also computed. Figure 14 shows the voltage between successive adjacent turns. This figure presents two sets of curves depending to the difference between the turn numbers. The higher turn-to-turn voltages are obtained for differences between the turn numbers of 5 (solid lines); they
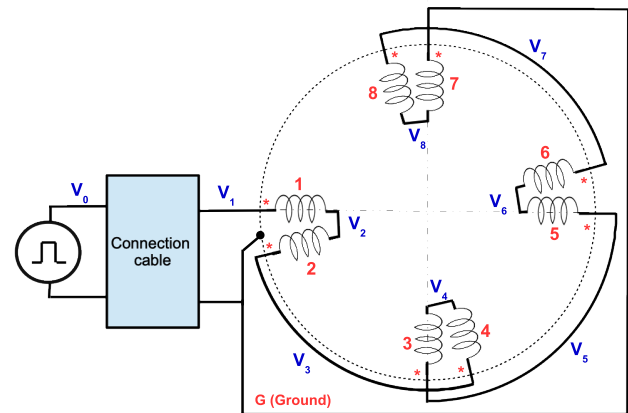

Figure 15: Motor phase coil connections for getting a 24-20-SRM.

are lower when this difference is 3 (dotted lines). For a $100\,V$ input pulse, the maximum peak voltage is $30\,V$ (30%) between turns 10 and 15 at the coil centre, for a steady state of $20.8\,V$ (5×4.16%). The results are very similar for a slightly larger distance between turns because the turn-to-turn capacitances decrease while all the self and mutual inductance increase.

5 Coil voltage estimation for an actual motor phase

5.1 Experimental approach

The voltage distribution between the stator coils during transients following the fast fronted voltages is measured experimentally. The 8 inorganic coils are placed on the stator teeth and connected as it is schematized in Figure 15. The star sign (*) denotes the coil winding direction: when a current enter in the star side, it creates a magnetic flux that enter in the corresponding stator tooth. The connections are made following the SRM 24-20 rules defined by the literature on fractional-slot concentrated-windings machines for providing a 20-pole rotating fundamental field when the stator is fed by a balanced 3-phase currents [20].

The experimental set-up consists of a high voltage pulse generator connected between the input of the motor phase (coil 1); its output (coil 7). The ground point of the pulse generator is connected to the output of the motor phase and to the frame. The connection cable length is $1\,m$. The voltage pulse must be over $360\,V$, which is the maximum pulse magnitude of the Phase-to-neutral voltage for a motor fed by a PWM inverter connected to a standard $540\,V$ dc bus.
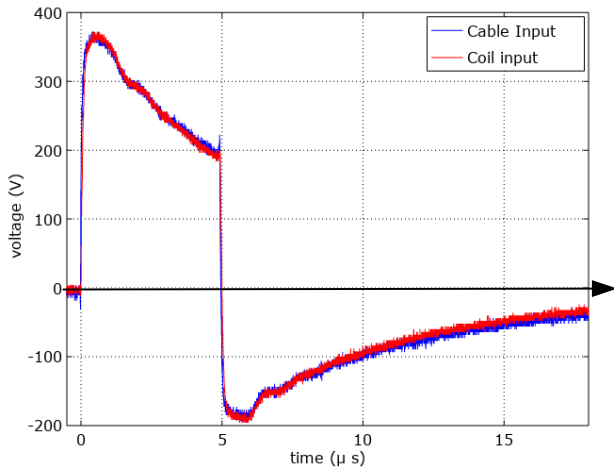
Figure 16: Input pulse used for measurements.

Figure 17: Transient voltage measurements at the coil level.

Measurements are made with a fast oscilloscope synchronized on the output voltage of the pulse generator (v_0 in Figure 15). For this channel, measurements are made with a $1/100 - 350\,MHz$ passive probe. The ground point of the oscilloscope is connected to the ground point of the generator. The motor coil-to-ground voltages $v_1 - v_8$ are measured with the same broadband differential probe ($100\,MHz$). The pulse generator is tuned for producing $400\,V - 4\,\mu s$ pulses at a frequency of $10\,kHz$. The time lag between pulses is long enough for demagnetizing the stator core. Figure 16 presents the input pulse in a large time window. It can be seen that the pulse produced by the generator is not perfect; its magnitude is only $370\,V$ for a generator tuned at $400\,V$ because of the generator internal impedance. The voltage drop increase with time because of the current increase. The pulse slew rate is $4.28\,kV/\mu s$ (the voltage reaches $300\,V$ in $70\,ns$).

Figure 17 shows the cable input voltage (v_0) and the voltages at each coil input ($v_1 - v_8$) in a time window corresponding the the transient state. The motor phase input voltage v_1 has a fast ac component due to the connection cable transient superimposed to the source pulse voltage v_0. The cable transient has a slight influence on v_2 but none on the other voltages that has a slower transient state.

A careful observation of Figure 17 shows that the waveforms are not classical damped sine waves with a natural angular frequency β, a damping factor α and a shift φ ($e^{-\alpha t}\sin(\beta t + \varphi)$). The system linearity must be tested. The same measurements were made for several pulse generator electromotive forces (emf). Figure 18 presents results. The coil-to-ground peak voltages are proportionals to the generator emf. Therefore, the system can be modelled by a linear equivalent circuit for voltages up to $450\,V$.
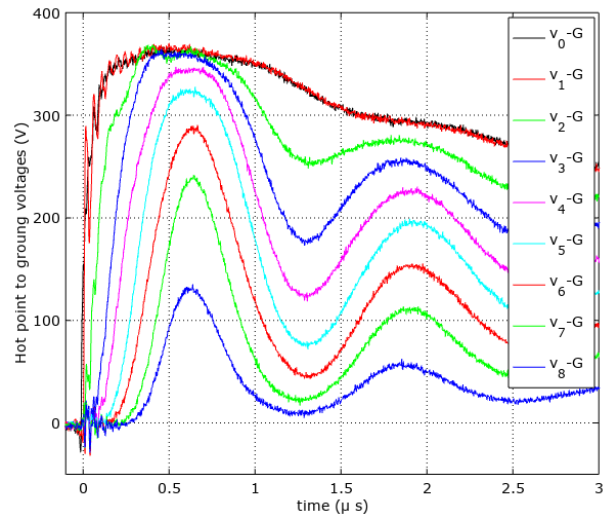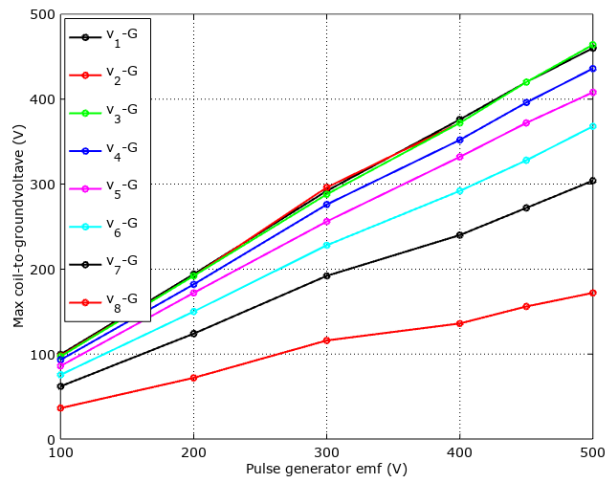

Figure 18: Peak voltage of the transient of each coil.

Figure 19 shows the voltages between the coil terminals. The first coil withstands a higher voltage than the other ones : $250\,V_{peak}$ rather than $\simeq 120\,V_{peak}$ for the others. This phenomena is the same for classical organic windings; the common mode capacitance (coil to ground) of the second coil remains uncharged during the pulse rise time; consequently, a large voltage appear at the terminals of the first coil during the very beginning of the transient.

5.2 Spice simulation

Figure 20 presents the Spice equivalent circuit of a motor phase. Every coil is modeled by RLC circuit; the resistance is computed considering the core HF losses; mutual inductances, which are not represented on the equivalent cir-
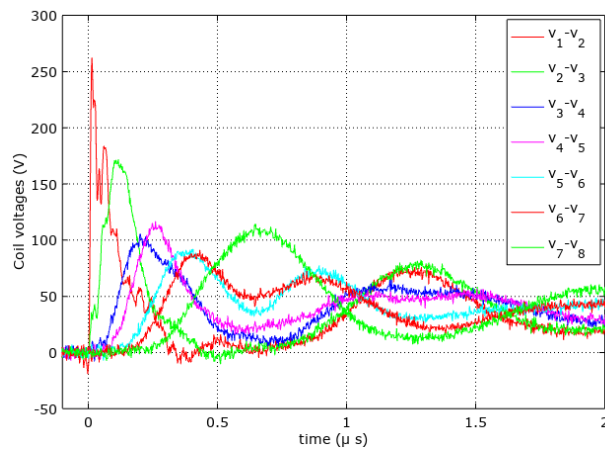
Figure 19: Transient voltage for each stator coil foe an actual pulse magnitide of 370 V.
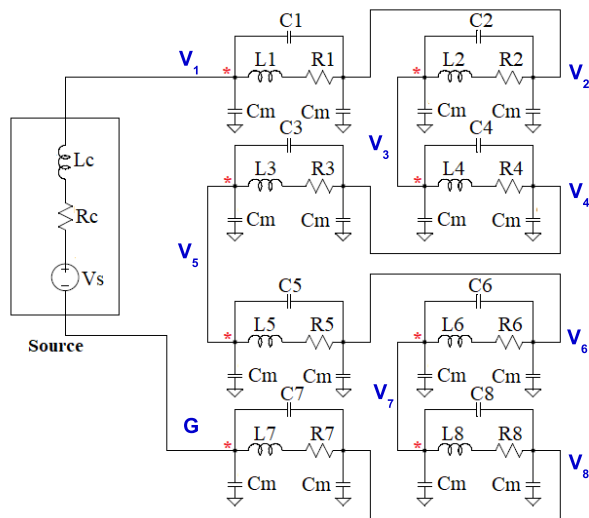

Figure 20: Spice equivalent circuit of a motor phase defined at the coil level.

Table 2: Self and mutual inductances relative to the first coil

	L_1	M_{12}	M_{13}	M_{14}
angle (°)	0	15	90	105
(μH)	116	−31	−2.6	−2.13
	M_{15}	M_{16}	M_{17}	M_{18}
angle (°)	180	195	270	275
(μH)	−2.0	−2.1	−2.6	−3.0

cuit, are taken into account. The magnetic core adds common mode capacitances, which are modelled by the capacitances C_m connected between each coil terminal and ground. The voltage measurement points ($v_1 - v_8$) defined in Figure 15 are reported in the Spice equivalent circuit.
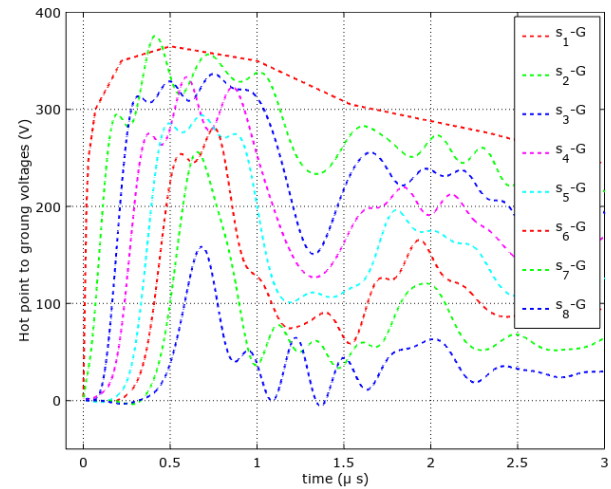

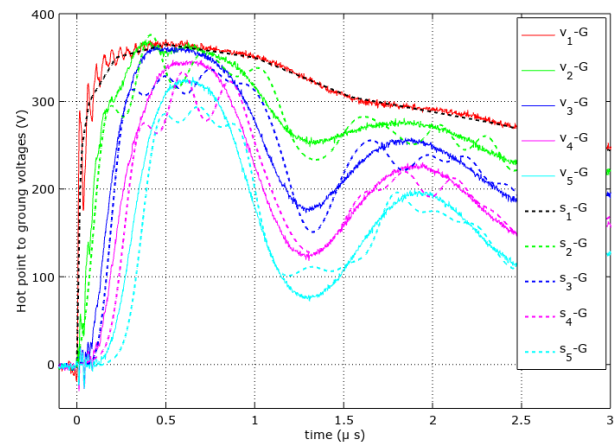**Figure 21:** Spice simulation results for a motor phase.

Figure 22: Comparison of Spice simulation results (dotted lines) and experimental ones (solid lines).

The parameters of the Spice equivalent circuit are measured with sine waves at 1 MHz; Table 2 presents the self and mutual inductances relatively to coil 1 and the corresponding coil relative angular position. With the sign convention adopted (⋆ signs in Figure 15) all the mutual inductances are negatives. The actual connections are considered in the Spice equivalent circuit in Figure 20. The self inductances of the other coils have the same value (116 μH); the mutual inductances relative to the other coils have also the values of Table 2 for identical relative angular positions.

The coil resistance takes the core losses into account. The common mode capacitances are measured with an impedance analyzer the average result is $C_m = 43\ pF$ with a measurements dispersion of about 5%. The actual waveform produced by the pulse generator is taken form experimental results; the Spice source voltage v_s is defined by

segments joining points extracted from the experimental curve v_0. Figure 21 presents the simulation results and Figure 22 compare the simulation results with the experimental ones.

6 Discussion

Figure 22 shows a global correspondence of Spice simulation results and measurements. However, differences are be observed on the damping of each transient voltage. These differences can be interpreted considering the equivalent circuit parameter, which are measured in sine waves. The Spice equivalent circuit uses them in the time domain, which supposes constant parameters in the frequency domain. The inductances and the capacitances measured values are nearly constant in the useful frequency range ($100\,kHz$ – $20\,MHz$) but not the resistances because of skin effects in the wire and in the stator core. The Spice simulation were made with average values that do not consider all the complexity of the electromagnetic problem.

However, the Spice simulation estimates the peak voltage at the terminals of each coil for making technological pertinent choices at the design level. It shows also that the transient state, for every coils, except the first one, are about $1\mu s$ long. They are 10 times shorter for the transient inside the coil defined at the turn level. Consequently the coils $2-8$ must withstand only $100\,V_{peak}$ for a machine phase fed by $370\,V$ pulses. Inside these coils, the maximum turn-to-turn voltage is only $30\,V_{peak}$, which is much under the capabilities of a ceramic coated wire operating at $500°C$, which is $200\,V_{RMS}$ [9]. However, a special care must be taken for the first coil that withstand $250\,V_{peak}$ during about $200\,ns$. The transient analysis made at the turn level (Figure 14) estimates that the turn-to-turn voltage at 30% of this value ($75\,V$), which remains under the limits with a large safety margin.

The proposed turn arrangement for designing coils can be used for machines fed by a standard PWM inverter, when the turn-to-turn voltage must be very low. With such a turn arrangement and standard organic low temperature wire, the motor can be fed by high voltages. For HT° applications, the coil design compensates the poor electrical properties of the ceramic-coated wire.

7 Conclusion

The design of high temperature compact machines requires a specific approach because the machine must be fully inorganic, without any polymer. The use of magnets is also forbidden. Consequently, the only possible topology is the synchronous reluctant machine made with one rigid inorganic coils per stator tooth. These coils are made with a ceramic insulated embedded in a HT° cement. The ceramic insulated wire has poor electrical and mechanical properties compared to the standard organic enamelled wire. These poor properties must be compensated by a specific topology that consists in making large number of transverse layers of few turn. The proposed topology is the opposite of the classical one consisting in building coils with a small number of longitudinal layers made of many turns.

After sharing the experience for building HT° motor coil, an analysis of the voltage distribution inside the coil, at the turn level, is proposed. The proposed method is based on a Spice solver. The results show a good voltage distribution between turns during the fast transients following each fast fronted voltage pulse of the PWM.

Another analysis, made at the coil level, shows that the first coil withstands higher voltages than the others at the very beginning of the transient states following the PWM fronts.

The global discussion on the results of the two analyses shows that the proposed coil topology can be used for building motors, fed by standard PWM inverters and able to operate up to $500°C$ inside coils.

References

[1] IEC 60172 Std., Test procedures for the determination of the temperature index of enameled and tape wrapped winding wires, 2015.

[2] Mitsui H., Progress in japan in electrical insulation at high temperatures, IEEE Electrical Insulation Magazine, 12, 3, May 1996, 16–27.

[3] Schadler L. S., Nelson J. K., Calebrese C., Travelpiece A., and Schweickart D. L., High temperature breakdown strength and voltage endurance characterization of nanofilled polyamideimide, In IEEE Transactions on Dielectrics and Electrical Insulation, 19, 6, Dec. 2012, 2090–2101.

[4] Hoang A. T., Serdyuk Y. V., and Gubanski S. M., Electrical characterization of a new enamel insulation, In IEEE Transactions on Dielectrics and Electrical Insulation, 21, 3, June 2014, 1291–1301.

[5] Aymonino F., Lebey T., Malec D., Petit C., Saint Michel J., and Anton A., Impact of the polymerization process on the electrical behavior of different impregnation varnishes, In proceedings of IEEE Conference on Electrical Insulation and Dielectric Phenomena, Oct. 2006, 728–731.

[6] Aymonino F., Lebey T., Malec D., Petit C., Michel J. S., Anton A., and Gimenez A., Degradation and dielectrics measurements of rotating machines insulation at high temperature (200-400°C), In proceedings of IEEE International Conference on Solid Dielectrics

(ICSD), July 2007, 130–133.

[7] Vonroll, Mica-taped wires samicafirewall, 2015, http://www. vonroll.com.

[8] CPG groupe Plastec, CERAFIL 500 - isolation céramique très haute température, Fiche technique, http://www.cables-cgp.com.

[9] Iosif V., Roger D., Duchesne S., and Malec D., Assessment and improvements of inorganic insulation for high temperature low voltage motors, In IEEE Transactions on Dielectrics and Electrical Insulation 23, 5, October 2016, 2534–2542.

[10] Takahashi N., Morishita M., Miyagi D., and Nakano M., Examination of magnetic properties of magnetic materials at high temperature using a ring specimen, In IEEE Transactions on Magnetics 46, 2, Feb. 2010, 548–551.

[11] Ababsa M., Ninet O., and Velu G., High temperature characterization of electrical steels using an adapted Epstein frame, In proceedings of IEEE International Magnetics Conference (INTERMAG), April 2017.

[12] Cozonac D., Babicz S., Ait-Amar-Djennad S., Velu G., Cavalini A., and Wang P., Study on ceramic insulation wires for motor windings at high-temperature, In proceedings of IEEE Conference on Electrical Insulation and Dielectric Phenomena (CEIDP), Oct 2014, 172–175.

[13] Cozonac D., Lecointe J.-P., Duchesne S., and Velu G., Materials characterization and geometry of a high temperature induction machine, In proceedings of International Conference on Electrical Machines (ICEM), Sept 2014, 2499–2505.

[14] Iosif V., Roger D., Takorabet N., Duchesne S., and Meibody-Tabar F., Technological assessments for designing machines able to work at very high internal temperatures (450–500°C), In proceedings of International Conference on Electrical Machines (ICEM), Sep. 2016, 2682–2687.

[15] Liu J., and Walmer M., Thermal stability and performance data for SmCo 2:17 high-temperature magnets on ppm focusing structures, In IEEE Transactions on Electron. Devices, 52, 5, May 2005, 899–902.

[16] Komeza K., Lefik M., Juszczak E. N., Roger D., Takorabet N., and Meibody-Tabar F., Analysis of the impact of the design of HT° machines on the cogging torque and losses in permanent magnets, In proceedings of IEEE International Conference on Power Electronics, Drives and Energy Systems (PEDES), Dec. 2016, 1–6.

[17] Marcin L., Komeza K., Napieralska-Juszczak E., Roger D., and Napieralski P., Comparison of the reluctance laminated and solid rotor synchronous machine operating at high temperatures, In COMPEL - The international journal for computation and mathematics in electrical and electronic engineering, 2019, https://www.emerald.com/insight/content/doi/10.1108/COMPEL-10-2018-0405/full/html.

[18] Roger D., Iosif V., and Duchesne S., High temperature motors: Investigations on the voltage distribution in windings at a short scale times for a PWM supply, In proceedings of IEEE International Electric Machines and Drives Conference (IEMDC), May 2017, pp. 1–7.

[19] Yokoi Y., Higuchi T., and Miyamoto Y., General formulation of winding factor for fractional-slot concentrated winding design, In IET Electric Power Applications 10, 4, 2016, 231–239.

[20] Pyrhonen J., Jokien T., and Hrabovcova V., Design of rotating electrical machines. Ed. John Wiley & Sons, 2008.

[21] Miller T. J. E., Electronic control of switched reluctance machines, Newnes power engineering series ed. 2001, http://www.new, espress.com.

[22] Kant M., Les actionneurs électriques pas à pas, Traité des nouvelles technologies, Série Automatique, 1989.

[23] Jufer M., Traité d'électricité Volume 9, Electromécanique, Presses polytechniques universitaires romandes, 2004.

[24] Elmadah H., Roger D., and Takorabet N., Définition du prototype d'une machine synchroréluctante haute temperature, In proceedings of Symposium de Genie Electrique (SGE), Juillet 2018.

[25] Cotronics, Adhesifs, ciments, revetements ceramiques hautes temperatures – 100 à 3000 deg., Fiche technique, http://www.cotronics.com.

[26] Roger D., Ninet O., and Duchesne S., Wide frequency range characterization of rotating machine stator-core laminations, In the European Physical Journal – Applied Physics (EPJ-AP) 23, 2, Aug. 2003, 103–109.

[27] McLyman W. T., Core Selection for Transformers and Inductors: A User's Guide to Practice and Specifications, 2018.